Quantitative Analysis on Geometric Size of LiDAR Footprint

Yongjun Zhang and Xiang Shen

***Abstract*—A light detection and ranging (LiDAR) footprint is the spot area illuminated by a single laser beam, which varies with the beam direction and the regional terrain encountered. The geometric size of the LiDAR footprint is one of the most critical parameters of LiDAR point cloud data. It plays a very important role in the high-precision geometric and radiometric calibration of LiDAR systems. This letter utilizes space analytic geometry to derive LiDAR footprint equations and strictly considers laser beam attitude and terrain slope. Compared to the conventional plane geometry solution, the proposed approach is not only more rigorous in theory but also more powerful in practical applications.**

***Index Terms*—Footprint, incidence angle, laser beam, light detection and ranging (LiDAR).**

I. Introduction

QUITE soon after the first working laser was invented and constructed in 1960, laser technology began to be widely applied to high-precision surveying and mapping. As early as the mid-1960s, laser altimeters were experimentally integrated to the airborne platform, which were mainly used for topographic mapping purposes [1]. However, it was not until the 1990s that commercial airborne laser scanners gradually started to mature owing to the emergence of long-lifetime diode-pumped solid-state lasers and direct georeferencing technology. After 20 years of rapid development, airborne laser scanning has been upgraded significantly, in both data acquisition efficiency and measurement accuracy. Nowadays, light detection and ranging (LiDAR) technology already is one of the most important large-scale topographic data acquisition methods and has become an invaluable tool in a wide range of subject matter, including agriculture, archaeology, forestry, geography, glaciology, and hydrology [2].

As an active remote sensing device, the LiDAR system has to emit electromagnetic waves in order to spot the target. The regional terrain illuminated by a single laser beam is commonly called the LiDAR footprint, which returns the reflected signal or energy back to the optical detector [3]. Apparently, LiDAR footprints that are larger in size lead to higher uncertainty on geometric positions [4], [5] and more complex backscattering responses. Therefore, the accurate calculation of the LiDAR footprint size is an essential prerequisite for both the high-precision geometric calibration [6] and radiometric calibration [7] of LiDAR systems.

Manuscript received January 20, 2013; revised May 23, 2013 and July 13, 2013; accepted July 25, 2013. This work was supported in part by the National Natural Science Foundation of China under Projects 41171292 and 41322010.

The authors are with the School of Remote Sensing and Information Engineering, Wuhan University, Wuhan 430079, China (e-mail: zhangyj@whu.edu.cn).

Color versions of one or more of the figures in this paper are available online at http://ieeexplore.ieee.org.

Digital Object Identifier 10.1109/LGRS.2013.2276126

The geometric shapes and sizes of LiDAR footprints are closely related to terrain conditions. To simplify the calculation in theoretical analysis, it is always assumed that the regional terrain is a perfect plane. In the early stage of airborne LiDAR research, Baltsavias [8] developed the first LiDAR footprint formulas for both a horizontal surface and a sloping terrain, which were widely adopted by many researchers thereafter [1], [9]. However, Baltsavias' equations are only applicable for across-track-scanning LiDAR systems (i.e., using polygonal or oscillating scanners). In a more recent work by Sheng [3], LiDAR footprint equations for both across-track and Palmer scanning (i.e., using monogon scanners) LiDAR systems were derived in detail. Although Sheng's approach was capable of yielding more accurate results compared to Baltsavias' approach, it still cannot be recognized as a rigorous method. The most critical issue is that these two methods both utilize plane analytic geometry to derive LiDAR footprint equations and are therefore only suitable for the special case of the terrain normal vector paralleling the scanning plane. Moreover, as the impacts of real flight attitude on LiDAR footprints are not considered by these approaches, they can only be used for theoretical analysis under ideal flying conditions. Unlike the previous methods, this letter employs space analytic geometry to deduce the LiDAR footprint equations; the real laser beam direction and the strict terrain slope definition are used in the formula derivations.

The remainder of this letter is organized as follows. The laser beam and its propagation characteristics are first briefly introduced. Then, we build the 3-D surface equations of the laser beam and the regional terrain and further solve the curve equation of the LiDAR footprint outline. In Section IV, a thorough comparison is conducted between the proposed approach and the existing methods. Finally, we present the experimental results in Section V and draw our concluding remarks in Section VI.

II. Laser Beam

As shown in Fig. 1, the outline shape of a LiDAR footprint is mainly determined by the propagation characteristics of the laser beam and the relative attitude of the laser beam w.r.t. the regional terrain. In this section, we only focus on the first influencing factor.

Topographic LiDAR systems typically use the Gaussian laser beam [10], which has a circular cross section, and its actual radius can be computed by

$$w_z = w_0 \left[1 + \left(\frac{M^2 \lambda z}{\pi w_0^2} \right)^2 \right]^{1/2} \tag{1}$$

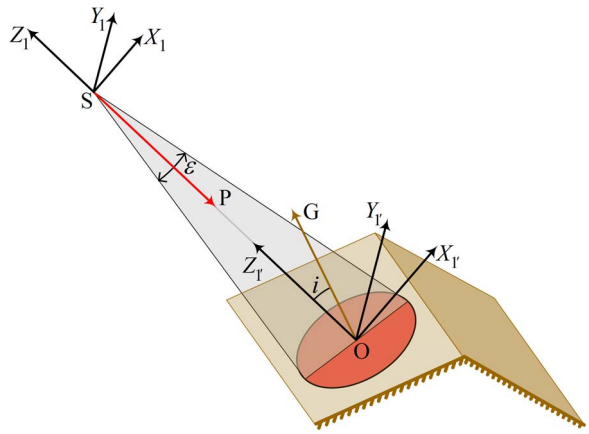

Fig. 1. LiDAR footprint and incidence geometry. $\overrightarrow{\mathrm{SP}}$ is the laser beam direction vector, $\overrightarrow{\mathrm{OG}}$ is the normal vector of the regional terrain plane, and ε and i are the beam divergence angle and the incidence angle, respectively.

where λ is the laser wavelength and M^2 is the laser beam quality factor. The geometric form of the beam vertical cross section defined by (1) is two hyperbolic lines. When $z = 0$, the laser beam radius w_z reaches a minimum value w_0, which is usually named as the beam waist radius [11], whereas when the z coordinate rises along the positive direction, w_z gradually increases toward infinity along the asymptotic lines. The included angle formed by two asymptotic lines is usually referred to as the beam divergence

$$\varepsilon = \lim_{z \to +\infty} \left[2 \arctan(w_z / z) \right]. \tag{2}$$

After arrangement, we can obtain the approximate formula of the laser beam radius at the far field

$$w_z = z \tan(\varepsilon/2). \tag{3}$$

In most scenarios, the measured objects are far away from the position of the LiDAR system. Therefore, only the propagation characteristics of the laser beam at the far field are truly concerned with the LiDAR footprint analysis. Theoretically, both (1) and (3) could be used to calculate the laser beam radius. However, as the hardware parameters supplied by LiDAR vendors generally do not include w_0 or M^2, (1) is usually unavailable for practical computation. Furthermore, almost all LiDAR hardware manufacturers do not explicitly provide the location of the laser beam waist; therefore, the z coordinate in (3) is generally approximated by the laser range observation r. Then

$$w_r = r \tan(\varepsilon/2). \tag{4}$$

Without loss of generality, only the ideal LiDAR system is considered in the subsequent analysis, which means that the laser beam waist position is coincident with the LiDAR optical center, and we will no longer distinguish between (3) and (4). In practice, if the beam waist position is accurately measured, then r in all the following formulas should be replaced by z.

III. LiDAR Footprint

A. Reference Frames

Before formally deriving the LiDAR footprint equations, we first define all the required reference frames and present the transformation relations between different frames. Table I shows all the reference frames used in this letter, where the l-frame is a sensor coordinate system which is defined by the laser beam direction vector (cf. Fig. 1) and the w-frame is a global object coordinate system used in a whole project. We introduce the symbol $\boldsymbol{R}_{\mathrm{l}}^{\mathrm{w}}$ to describe the transformation matrix from the l-frame to the w-frame, which is calculated from combining the instantaneous scan angle, flight attitude, and boresight angles [1], [5]. The g-frame is defined by the normal vector of the regional terrain plane, and the attitude transformation matrix from the w-frame to the g-frame can be computed by

TABLE I
Required Reference Frames

ID	Description
l	Laser beam frame. Its origin is the optical center of the LiDAR system, and its Z-axis points to the negative direction of the laser beam direction vector.
g	Regional ground frame. Its origin is the incidence point of the laser beam direction vector on the regional terrain plane, and its Z-axis is defined by the terrain normal vector.
w	World frame.
l′	An auxiliary frame. Its origin is the same as the g-frame, and its axis directions are the same as the l-frame.
l″	An auxiliary frame. The directions of its X and Y axes correspond to those of the l′-frame rotated by a specific angle around the Z-axis.
g′	An auxiliary frame. The directions of its X and Y axes correspond to those of the g-frame rotated by a specific angle around the Z-axis.

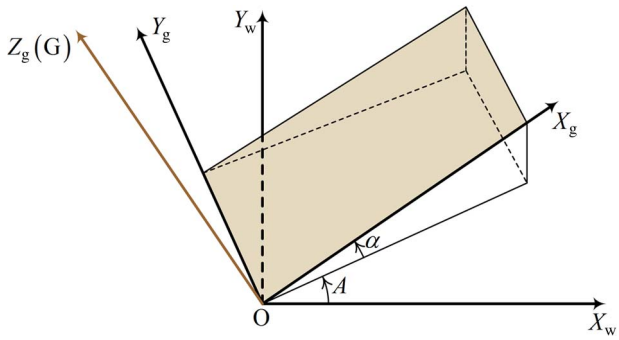

Fig. 2. Geometric description of the regional terrain plane. The first rotation is the azimuth A around the Z-axis, and the second rotation is the elevation angle α around the Y-axis.

$$\boldsymbol{R}_{\mathrm{w}}^{\mathrm{g}} = \boldsymbol{R}_Y(\alpha)\boldsymbol{R}_Z(A) \tag{5}$$

where A and α are the azimuth and the elevation angle (cf. Fig. 2) of the regional terrain plane, respectively. Then, the rotation relation between the l-frame and the g-frame can be given by

$$\boldsymbol{R}_{\mathrm{l}}^{\mathrm{g}} = \boldsymbol{R}_{\mathrm{w}}^{\mathrm{g}} \boldsymbol{R}_{\mathrm{l}}^{\mathrm{w}}. \tag{6}$$

In order to detail the coordinate transformation relation between the l-frame and the g-frame, we further introduce three auxiliary coordinate systems (i.e., the l′-frame, l″-frame, and g′-frame). These auxiliary frames all have the same coordinate origins as the g-frame but use different axis directions. As shown in Table I, the axis directions of the l′-frame are identical

to those of the l-frame. Therefore, the coordinates in the l′-frame and the g-frame will satisfy

$$\begin{bmatrix} X_{\mathrm{l}'} \\ Y_{\mathrm{l}'} \\ Z_{\mathrm{l}'} \end{bmatrix} = \boldsymbol{R}_{\mathrm{g}}^{\mathrm{l}} \begin{bmatrix} X_{\mathrm{g}} \\ Y_{\mathrm{g}} \\ Z_{\mathrm{g}} \end{bmatrix} = \left(\boldsymbol{R}_{\mathrm{l}}^{\mathrm{g}}\right)^{\mathrm{T}} \begin{bmatrix} X_{\mathrm{g}} \\ Y_{\mathrm{g}} \\ Z_{\mathrm{g}} \end{bmatrix}. \tag{7}$$

Note that, if the rotation matrix $\boldsymbol{R}_{\mathrm{g}}^{\mathrm{l}}$ is decomposed to a triple of Euler angles with the Z-X-Z convention [12], then (7) could be converted to

$$\begin{bmatrix} X_{\mathrm{l}'} \\ Y_{\mathrm{l}'} \\ Z_{\mathrm{l}'} \end{bmatrix} = \boldsymbol{R}_Z(\kappa)\boldsymbol{R}_X(i)\boldsymbol{R}_Z(\varphi) \begin{bmatrix} X_{\mathrm{g}} \\ Y_{\mathrm{g}} \\ Z_{\mathrm{g}} \end{bmatrix}. \tag{8}$$

According to the definitions of the l″-frame and the g′-frame in Table I, (8) can be further arranged to

$$\begin{aligned} \begin{bmatrix} X_{\mathrm{l}''} \\ Y_{\mathrm{l}''} \\ Z_{\mathrm{l}''} \end{bmatrix} &= \boldsymbol{R}_Z^{\mathrm{T}}(\kappa) \begin{bmatrix} X_{\mathrm{l}'} \\ Y_{\mathrm{l}'} \\ Z_{\mathrm{l}'} \end{bmatrix} \\ &= \boldsymbol{R}_X(i)\boldsymbol{R}_Z(\varphi) \begin{bmatrix} X_{\mathrm{g}} \\ Y_{\mathrm{g}} \\ Z_{\mathrm{g}} \end{bmatrix} = \boldsymbol{R}_X(i) \begin{bmatrix} X_{\mathrm{g}'} \\ Y_{\mathrm{g}'} \\ Z_{\mathrm{g}'} \end{bmatrix} \\ &= \begin{bmatrix} 1 & 0 & 0 \\ 0 & \cos i & -\sin i \\ 0 & \sin i & \cos i \end{bmatrix} \begin{bmatrix} X_{\mathrm{g}'} \\ Y_{\mathrm{g}'} \\ Z_{\mathrm{g}'} \end{bmatrix} \\ &= \begin{bmatrix} X_{\mathrm{g}'} \\ \cos i Y_{\mathrm{g}'} - \sin i Z_{\mathrm{g}'} \\ \sin i Y_{\mathrm{g}'} + \cos i Z_{\mathrm{g}'} \end{bmatrix}. \end{aligned} \tag{9}$$

B. Geometric Equations

From the analysis in Section II, we know that the cross section of a Gaussian laser beam is a circle. Therefore, the laser beam outline in the l-frame could be expressed as a conical surface equation based on (4)

$$X^2 + Y^2 = Z^2 \tan^2(\varepsilon/2). \tag{10}$$

The coordinate origin of the l-frame is different from that of the l′-frame, but the axis directions are the same. Therefore, the geometric equation of the laser beam cone in the l′-frame is

$$X_{\mathrm{l}'}^2 + Y_{\mathrm{l}'}^2 = (Z_{\mathrm{l}'} - r)^2 \tan^2(\varepsilon/2). \tag{11}$$

As the rotation relation around the Z-axis is the only difference between the l′-frame and the l″-frame, the geometric form of (11) will remain unchanged in the l″-frame. Then

$$X_{\mathrm{l}''}^2 + Y_{\mathrm{l}''}^2 = (Z_{\mathrm{l}''} - r)^2 \tan^2(\varepsilon/2). \tag{12}$$

Note that the transformation relation between the coordinates in the l″-frame and the g′-frame is described by (9). Therefore, if (9) is substituted into (12), we will get the geometric equation of the laser beam cone in the g′-frame

$$\begin{aligned} &X_{\mathrm{g}'}^2 + (\cos i Y_{\mathrm{g}'} - \sin i Z_{\mathrm{g}'})^2 \\ &\qquad = (\sin i Y_{\mathrm{g}'} + \cos i Z_{\mathrm{g}'} - r)^2 \tan^2(\varepsilon/2). \end{aligned} \tag{13}$$

The curve equation of the LiDAR footprint can be obtained by combining the 3-D surface equations of the laser beam and the regional terrain plane together. According to the definition of the g′-frame, the geometric equation of the regional terrain plane can be expressed as

$$Z_{\mathrm{g}'} = 0. \tag{14}$$

By substituting (14) into (13) and arranging terms, we can get

$$\begin{aligned} &X_{\mathrm{g}'}^2 + \left(Y_{\mathrm{g}'} K^{1/2} + \sin i \tan^2(\varepsilon/2) K^{-1/2} r\right)^2 \\ &\qquad = \left(\cos i \tan(\varepsilon/2) K^{-1/2} r\right)^2 \end{aligned} \tag{15}$$

where $K = \cos^2 i - \sin^2 i \tan^2(\varepsilon/2)$. It can be seen from (15) that the geometric form of the LiDAR footprint in the g′-frame is an ellipse, and its center is not located in the incidence point O (cf. Fig. 3). Finally, the curve equation of the LiDAR footprint is transformed from the g′-frame to the g-frame. As the rotation around the Z-axis is only one difference between the g′-frame and the g-frame, the elliptical center coordinates and the ellipse axis directions will be altered, but the geometric shape and size of the laser footprint will remain unchanged (cf. Fig. 3).

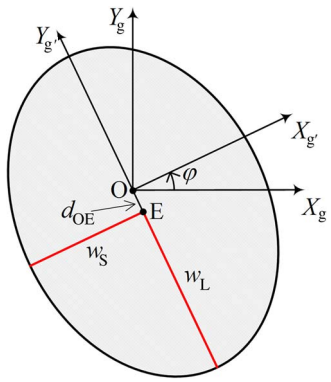

Fig. 3. LiDAR footprint in the g-frame and g′-frame. E is the center of the footprint ellipse, and w_{L} and w_{S} are the major and minor radii, respectively.

In the closed interval of $[-\pi, \pi]$, the angle i in (15) has two different sets of effective value range, $0 \le |i| < (\pi - \varepsilon)/2$ and $(\pi + \varepsilon)/2 < |i| \le \pi$, whereas when $(\pi - \varepsilon)/2 \le |i| \le (\pi + \varepsilon)/2$, there is no real solution. As shown in Fig. 4, i is actually the incidence angle between the laser beam direction vector and the terrain normal vector, and the three groups of value range correspond to the different incidence geometry scenarios. When the laser beam and the terrain normal vector are located in the same side w.r.t. the regional terrain, a limited size of the LiDAR footprint ellipse can be obtained by the intersection. The major and minor radii of the footprint ellipse can be readily derived from (15)

$$\begin{cases} w_{\mathrm{L}} = \cos i \tan(\varepsilon/2) K^{-1} r \\ w_{\mathrm{S}} = \cos i \tan(\varepsilon/2) K^{-1/2} r. \end{cases} \tag{16}$$

It is also very easy to calculate the distance between the incidence point O and the footprint ellipse center E

$$d_{\mathrm{OE}} = \sin i \tan^2(\varepsilon/2) K^{-1} r. \tag{17}$$

In the second scenario, when the laser beam and the terrain normal vector are located in the different sides w.r.t. the regional

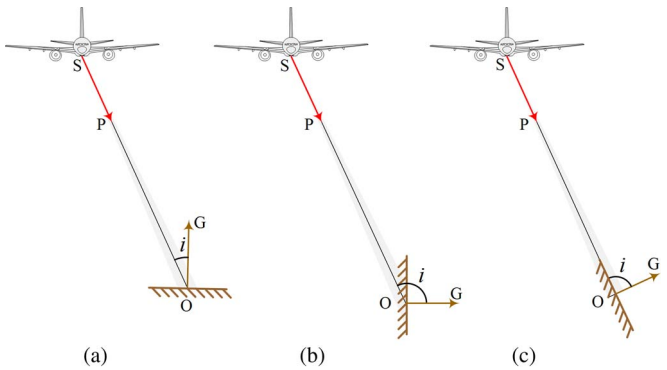

Fig. 4. Three incidence geometry conditions. The laser beam and terrain normal vector are located in (a) the same side and (b) the different sides w.r.t. the regional terrain. (c) Regional terrain is in the covering area of the laser beam cone.

terrain, there is no LiDAR footprint formed in the current terrain region, and in the last scenario, when the regional terrain is located in the covering area of the laser beam cone, the theoretical LiDAR footprint size will reach an infinite value. However, as it is impossible for the real terrain to be a perfect plane, this scenario will never occur in real-world situations.

IV. Discussion

Compared with previous approaches [3], [8], the proposed method has several advantages.

1) Using real laser beam attitudes. The existing equations only consider the influence of the instantaneous scan angle on LiDAR footprints. Therefore, they can only be used in the theoretical analysis under ideal flight conditions. The proposed method employs the real laser beam attitude to derive the equations, which could be used directly for the LiDAR footprint calculations with the real point cloud data. For the case of airborne LiDAR, the proposed equations are not limited to a specific scanning mechanism, and they also could be applied directly to the tilt-mount LiDAR systems.
2) Suitability for general geometric conditions. The existing literature reports the use of plane analytic geometry to deduce LiDAR footprint formulas and is therefore only suitable for the special case of the terrain normal vector paralleling the scanning plane. In the special scenario shown in Fig. 5, the incidence angle, instantaneous scan angle, and elevation angle meet $i = \theta - \alpha$. AB is the major axis of the footprint ellipse, and its length can be calculated by plane geometry equations. However, if the terrain rotates an angle around AB, then the terrain normal vector OG will obliquely intersect the scanning plane SNO. Then, $i \neq \theta - \alpha$, and AB is no longer the major axis of the footprint ellipse. Consequently, the LiDAR footprint formulas deduced by the plane analytic geometry are not applicable anymore.
3) Using rigorous formulas. Even in the special case in Fig. 5, Sheng's equations are still not theoretically accurate, although the errors are trivial. Note that $i = \theta - \alpha$ and $r = H/\cos\theta$ in Fig. 5; then, Sheng's equations can be given by

$$\begin{cases} w_{\mathrm{L}} = \frac{\cos i \sin\varepsilon}{\cos(2i)+\cos\varepsilon} r = \cos i \tan(\varepsilon/2) K^{-1} r \\ w'_{\mathrm{S}} = \tan(\varepsilon/2) r. \end{cases} \tag{18}$$

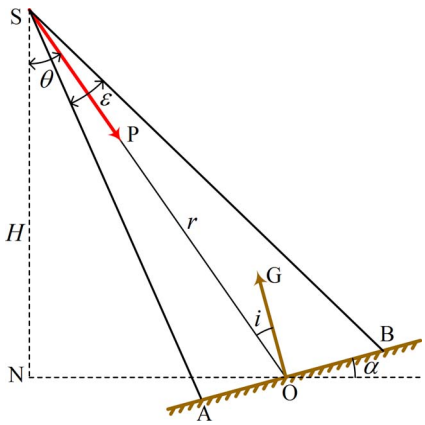

Fig. 5. Special case of incidence geometry. The laser beam direction vector is only determined by the instantaneous scan angle θ, and the terrain normal vector $\overrightarrow{\mathrm{OG}}$ is strictly parallel to the scanning plane SNO.

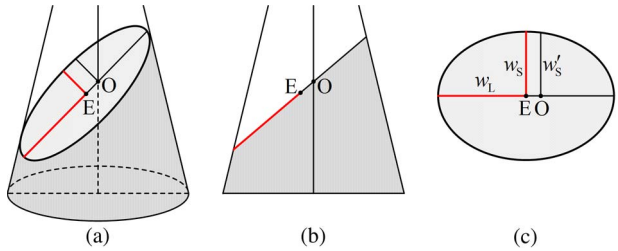

Fig. 6. Geometric shape of the LiDAR footprint. (a) Perspective view. (b) Side view. (c) Top view taken from the terrain normal vector.

Compared to (16), it could be found that the minor radius of the LiDAR footprint ellipse in Sheng's equations is a constant w.r.t. i, which is different from our proposed equations. This is because the "minor radius w'_{S}" calculated by Sheng's formulas is actually the transversal length of the incidence point O. As shown in (15) and Fig. 6, if the regional terrain plane obliquely intersects with the laser beam, O does not locate in the geometric center of the LiDAR footprint ellipse. Fig. 7 further illustrates that the major radius, the minor radius, and the center offset of the footprint ellipse all increase toward infinity as the incidence angle i approaches $(\pi - \varepsilon)/2$, but the change rates of the latter two parameters are quite slow, which proves that the errors of Sheng's equations are trivial in the special incidence geometry case in Fig. 5. Baltsavias [8] only provided the major radius equation of the LiDAR footprint, which is different from our proposed equation and is given by

$$w'_{\mathrm{L}} = \frac{H \sin(\varepsilon/2)\left(\cos i + \sin i \tan(i + \varepsilon/2)\right)}{\cos(\theta - \varepsilon/2)}. \tag{19}$$

As shown in Fig. 7, w'_{L} is clearly not correct because it does not hold the special case of $i = 0$, which was previously reported and discussed in detail by Sheng [3].

V. Experiments

Two experiments using real and simulated data were conducted to quantify the differences between our proposed and Sheng's LiDAR footprint equations in general geometric

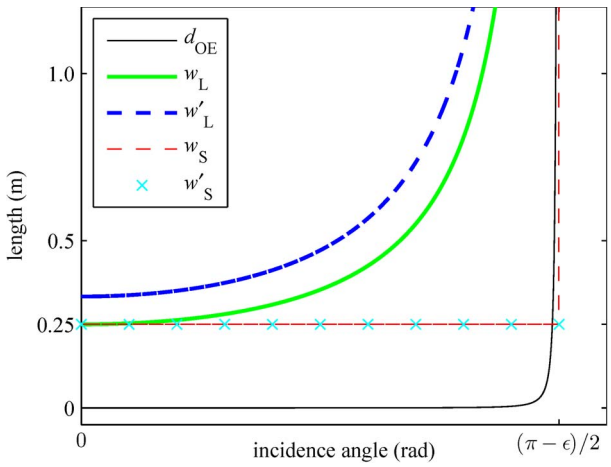

Fig. 7. Influence of incidence angle on the geometric shape and position of the LiDAR footprint. In this simulated scenario, $\varepsilon = 1$ mrad, $r = 500$ m, and $\theta = 30^\circ$.

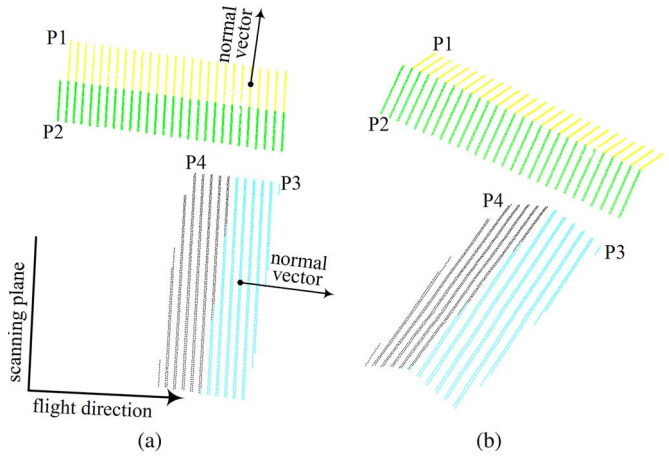

Fig. 8. Small study area with two gable buildings. P1–P4 represent different roof planes. (a) Top view. (b) Perspective view.

conditions. As depicted in Fig. 8, two LiDAR points located in different gable roofs were chosen to calculate their footprint sizes in the real data experiment. For the LiDAR point in the plane P1, the differences in the major and minor radii between the results of Sheng's and our proposed methods are 4.2% and 1.1%, respectively; as for the LiDAR point in P3, the differences are -6.6% and 1.0%, respectively. According to our analysis in Section IV, the errors in Sheng's results mainly originate from two reasons. On the one hand, Sheng's equations only consider the instantaneous scan angle. However, in real flight conditions, the scanning platform is usually not exactly level, and the sensor tilt angles also affect the LiDAR footprint sizes. This issue can cause an almost constant error to these two LiDAR points in different roofs because they are located in the same scan line, and accordingly, the corresponding tilt angles are nearly the same. On the other hand, Sheng's equations are only suitable for the special geometric scenario of the terrain normal vector paralleling the scanning plane, which can explain the considerable variation of the major radius errors between the LiDAR points in the planes P1 and P3.

To better characterize the error variations of Sheng's equations in general geometric conditions, simulated data were also adopted in our experiment. An ideal horizontal scanning platform was simulated, which aims to isolate the influence of sensor tilt angles. The experimental results show that the major and minor radii of LiDAR footprints calculated by Sheng's equations are almost the same as those of our proposed equations when the terrain normal vector is parallel to the scanning plane. In general geometric scenarios, only the major radius results of Sheng's equations are not accurate. The errors reach the maximum when the horizontal component of the terrain normal vector is vertical to the scanning plane, and the value is as much as -13.4% when the elevation angle equals 30°.

VI. Conclusion

The geometric shape and size of LiDAR footprints are collectively determined by the laser beam propagation itself and its relative attitude relation with the regional terrain encountered. In this letter, we have rigorously defined the space equations of the laser beam and further derived LiDAR footprint formulas based on the space analytic geometry. Our proposed approach addresses the technical deficiencies of the existing plane geometry algorithms, i.e., only suitable for the special case of incidence geometry and the ideal flight condition, and it can be easily applied to practical applications.

References

[1] J. Shan and C. K. Toth, *Topographic Laser Ranging and Scanning: Principles and Processing*. Boca Raton, FL, USA: CRC Press, 2008.
[2] G. L. Heritage and A. R. G. Large, *Laser Scanning for the Environmental Sciences*. Chichester, U.K.: Wiley-Blackwell, 2009.
[3] Y. Sheng, "Quantifying the size of a LiDAR footprint: A set of generalized equations," *IEEE Geosci. Remote Sens. Lett.*, vol. 5, no. 3, pp. 419–422, Jul. 2008.
[4] D. D. Lichti, S. J. Gordon, and T. Tipdecho, "Error models and propagation in directly georeferenced terrestrial laser scanner networks," *J. Surv. Eng.*, vol. 131, no. 4, pp. 135–142, Nov. 2005.
[5] T. Goulden and C. Hopkinson, "The forward propagation of integrated system component errors within airborne LiDAR data," *Photogramm. Eng. Remote Sens.*, vol. 76, no. 5, pp. 589–601, May 2010.
[6] R. V. Ussyshkin, R. Ravi, M. Ilnicki, and M. Pokorny, "Mitigating the impact of the laser footprint size on airborne LiDAR data accuracy," in *Proc. ASPRS Annu. Conf.*, Baltimore, MD, USA, 2009, pp. 854–862.
[7] W. Y. Yan, A. Shaker, A. Habib, and A. P. Kersting, "Improving classification accuracy of airborne LiDAR intensity data by geometric calibration and radiometric correction," *ISPRS J. Photogramm. Remote Sens.*, vol. 67, pp. 35–44, Jan. 2012.
[8] E. P. Baltsavias, "Airborne laser scanning: Basic relations and formulas," *ISPRS J. Photogramm. Remote Sens.*, vol. 54, no. 2/3, pp. 199–214, Jul. 1999.
[9] J. C. Brock, C. W. Wright, A. H. Sallenger, W. B. Krabill, and R. N. Swift, "Basis and methods of NASA airborne topographic mapper LiDAR surveys for coastal studies," *J. Coastal Res.*, vol. 18, no. 1, pp. 1–13, 2002.
[10] J. B. Blair, D. L. Rabine, and M. A. Hofton, "The Laser Vegetation Imaging Sensor: A medium-altitude, digitisation-only, airborne laser altimeter for mapping vegetation and topography," *ISPRS J. Photogramm. Remote Sens.*, vol. 54, no. 2/3, pp. 115–122, Jul. 1999.
[11] J. Alda, "Laser and Gaussian beam propagation and transformation," in *Encyclopedia of Optical Engineering*, R. Driggers, Ed. New York, NY, USA: Marcel Dekker, 2003, pp. 999–1013.
[12] J. Diebel, *Representing Attitude: Euler Angles, Unit Quaternions, and Rotation Vectors*. Stanford, CA, USA: Stanford Univ., 2006. [Online]. Available: http://www.swarthmore.edu/NatSci/mzucker1/e27/diebel2006attitude.pdf